Applied Acoustics 224 (2024) 110132

Contents lists available at ScienceDirect

Applied Acoustics

journal homepage: www.elsevier.com/locate/apacoust

Active acoustic measurement of sound speed for quantifying underwater gaseous bubble emissions

Shuduo Liu [a], Jianghui Li [b,*], Wen Xu [a,c]

[a] College of Information Science and Electronic Engineering, Zhejiang University, Hangzhou 310027, China
[b] State Key Laboratory of Marine Environmental Science, College of Ocean and Earth Sciences, Xiamen University, Xiamen 361102, China
[c] Zhejiang Provincial Key Laboratory of Ocean Observation-Imaging Testbed, Ocean College, Zhejiang University, Zhoushan 316036, China

ARTICLE INFO

Keywords:
Underwater gas leakage monitoring
Numerical model
Sound speed quantification
Inversion
Underwater active acoustics
Bubble size distribution

ABSTRACT

Artificial or natural processes can cause underwater gas leakage, which often forms upwelling bubbly plume. The interaction of gaseous plume with acoustic waves would result in the variation of sound speed, which makes it possible to monitor the upwelling process via active acoustics. In this work, we build a numerical model to simulate the transport of gaseous bubbles and the sound speed response to the plume in the acoustic channel. The effectiveness of the model is validated by conducting a tank-based experiment, in which the sound speed variations were measured by varying gas flow rates. Meanwhile, signals at six frequencies (1 to 8 kHz) were transmitted and propagated through the medium part of which was occupied by the gaseous plume. Moreover, the comparison results also give a matched bubble size distribution (BSD), which further confirms the validity of the proposed model.

1. Introduction

Underwater gas leakage introduced by artificial or natural processes such as hydrothermal vents and marine carbon storage often forms upwelling bubble streams or even plumes [2,6]. The gaseous bubbles can influence the acoustic properties of the propagating medium, such as the sound speed and attenuation, and can thus be monitored via active acoustics.

In the past decades, researchers have actively investigated underwater acoustic propagation through a bubbly medium, both in theory and experiment. Foldy et al. [17] studied the multiple scattering theory and applied it to determine the total sound field of acoustic wave ensonifying a cloud of bubbles. The model takes the interaction of the incident acoustic wave and scattered acoustic wave of each bubble into account, then the total sound field being the average over all the mean-squared pressure fields of the bubble configuration. Wijngaarden et al. [45] extended the theory of Foldy into the nonlinear case. By applying the specific asymptotic limit to microscopic equations, the same result was obtained by Caflisch et al. [5]. Building upon the works of Wijngaarden et al. and Caflisch et al., Commander and Prosperetti [10] formulated a rigorous model for pressure waves propagating in a bubbly mixture. They incorporated a precise description of bubble internal dynamics [34] and derived the effective acoustic wave number from this model. Another approach to formulate the sound speed and attenuation perturbation imposed by bubbles was derived by Medwin and Clay [29,30] from the perspective of effective density and effective compressibility of bubble water mixture. This approach ignored the multiple scattering among bubbles; with low gas void fraction and non-uniform bubble size distribution (BSD), the multiple scattering effects are weak, as indicated by Feulliade et al. [16]. Consequently, the effective compressibility theory provides a computationally inexpensive alternative to the Foldy's multiple scattering theory (also used in our work presented in this paper). The relevant theories regarding sound speed variations in bubbly mixtures have been testified by several reports that directly measure sound speed. Commander and Prosperetti [10] conducted a detailed analysis on five different data sets obtained by Silberman [40], followed by Fox et al. [18], Kol'tsova et al. [20], Macpherson [27], and Ruggles et al. [38] to use their model. They concluded that the theory agrees with experimental data for polydisperse mixtures, but the agreement deteriorates at the resonance of bubbles for monodisperse mixtures. Buckingham [4] analyzed sound speed data in the sea surface bubble layer measured by Farmer and Vagle [15], and developed a model based on effective compressibility theory to describe the inverse-square sound speed profile. Wilson et al. [46] in-

* Corresponding author.
E-mail address: jli@xmu.edu.cn (J. Li).

https://doi.org/10.1016/j.apacoust.2024.110132
Received 7 November 2023; Received in revised form 15 April 2024; Accepted 14 June 2024
Available online 25 June 2024

vestigated the variation of sound speed caused by air bubbles with radii centered at 0.62 mm. They utilized a novel instrument based on the transfer-function technique to perform sound speed measurements around the bubble resonance frequency. Their findings showed that the sound speed and attenuation at resonance were highly sensitive to the BSD, which is consistent with the conclusion of Commander and Prosperetti [10]. Duro et al. [12] conducted an experiment measuring sound speed and attenuation. They used a high-pressure washer to inject air bubbles into a large water-filled tank and transmitted acoustic waves through the bubbly water using a broadband transducer (30 - 170 kHz). The BSD obtained from optical measurements and deduced by matching theoretical and experimental attenuation exhibited good agreement. Cheyne et al. [8] measured the sound speed in bubbly water by measuring the reflection coefficient of an air/bubbly water interface. They found that the general profile of the measured sound speed agrees better with the theories at higher void fraction. Esposito et al. [13] introduced an innovative methodology termed the three pressure transducers (3PT) technique, designed to derive sound speed by gauging pressure fluctuations at three distinct locations. This technique was validated through experiments conducted on an air-water mixture with a predefined void fraction, yielding speed of sound measurements that closely aligned with the theoretical framework described in [3]. Nonetheless, the applicability of the 3PT technique is potentially limited by its foundational assumption that the acoustic pressure field can be modeled as a composite of both forward and backward traveling waves which may not hold in complex real-world aquatic environments, thereby potentially constraining the broader utility of this technique. Reeder et al. [35] conducted an investigation into the sound speed within an estuarine front at Mobile Bay, employing the technique of matched filtering applied to linear frequency-modulated signals of 1-second duration across a bandwidth of 10 to 100 kHz. The study further delineated the signals into two sub-bands, specifically 10-20 kHz and 20-80 kHz, for the purpose of estimating sound speed within these distinct frequency ranges. The findings from their research suggest that the observed sound speeds align closely with established theoretical frameworks when considered in the context of band-average values. Sojahrood et al. [42] conducted a study to investigate the impact of pressure on the speed of sound and its attenuation in bubbly water. They created uniform lipid-coated bubbles and transmitted a broadband pulse with a center frequency of 2.25 MHz through these bubbles. The attenuation and sound speed were determined by analyzing the changes in the power and phase spectra of the signals received before and after the bubbles were introduced. They found the previously developed models based on Caflisch equation [5] is the significant overestimation of the attenuation at the bubble resonance at higher void fractions and enhanced the model by including bubble-bubble interaction. These measurements of sound speed in bubbly medium exhibit inconsistency of the theories, and reveals the rationality of modeling sound speed and attenuation variation imposed by bubbles. While based on these existing models, to predict and quantify underwater gas leakage, a model would be possible to build.

In this paper, we incorporate the dynamic generation and transport of underwater gaseous bubbles to build such a model. First, the model simulates a gaseous bubbly with various radii and positions. We then consider acoustic waves' interaction with the bubbly medium in a certain volume and calculate the sound speed based on the effective compressibility theory proposed by Medwin and Clay [29,30]. To validate the model, we designed an experiment in an anechoic water tank quantifying the frequency-dependent sound speed and attenuation changes by varying the gas flow rates. In the experiment, air stone diffusers were used to generate bubbles and simulate the underwater gas plume. A flow meter was connected to the air pump to record the gas flow rate. To investigate the sound speed variation as a function of frequency and gas flow rate, the transmitted acoustic waves were modulated by Linear Frequency Modulated (LFM) at various frequency bands. To further match the model output with the acoustic measurements, a BSD inversion algorithm is developed.

The rest of the paper is organized as follows. The numerical model for sound speed variation from underwater gas emission, including the bubble plume formation, theory of sound speed variation and model structure, is presented in Section 2. Section 3 elaborates the methods for measuring underwater sound speed. The experimental settings and processes are presented in Section 4. The results are shown in Section 5 and discussed in Section 6. Finally, Section 7 concludes the paper.

2. Theoretical framework

The numerical model for the response of water sound speed and attenuation to gas plume (Fig. 1) [25] is composed of three components. In the bubble plume generation part, the presence of underwater gas emission is modeled as an assemblage of bubbles, moving randomly in the horizontal direction and accelerating in the vertical direction until reaching the water surface or dissipated, in which each bubble obeys the gas transport mechanism proposed by Leifer et al. [23,21]. The water column partly occupied by these simulated bubbles forms the acoustic channel. To calculate the theoretical sound speed and attenuation in the bubbly media, the effective compressibility approach, proposed by Medwin et al. [29,30], is applied.

2.1. Bubble plume generation

In the model, as the time instance updates, a certain quantity of spherical bubbles are added into the underwater plume with random initial radii r and horizontal locations (x, y). The two random variables are drawn from the BSD and bubble-generating location distribution, respectively.

Consider a bubble, of volume $V = 4\pi r^3/3$, whose internal pressure is P_{B}, containing N mols of gas at a temperature T in degrees Celsius, the ideal gas law at isothermal conditions has the form of:

$$V\frac{\partial P_{\mathrm{B}}}{\partial t} + P_{\mathrm{B}}\frac{\partial V}{\partial t} = RT\frac{\partial N}{\partial t}, \tag{1}$$

where R represents the universal gas constant. The internal bubble pressure P_{B} has three components: the atmospheric partial pressure P_{A}, the hydrostatic pressure, and the Laplace pressure, which can be expressed as:

$$P_{\mathrm{B}} = P_{\mathrm{A}} + \rho_{\mathrm{w}} g z + 2\sigma/r, \tag{2}$$

where ρ_{w} denotes the density of surrounding water, z denotes the depth of the bubble, g denotes the local gravity, and σ denotes the surface tension. Fick's law can be used to express the gas flux (mols/unit area), F, across a boundary as:

$$F = k_{\mathrm{B}}\left(C - \frac{P_{\mathrm{B}}}{H}\right), \tag{3}$$

where k_{B} denotes the gas transfer velocity, C denotes the aqueous concentration, and H denotes the Henry's law constant [23]. Thus combining (2) and (3) one obtains an expression for the rate of gas loss in the bubbles, which is given by

$$\frac{\partial N}{\partial t} = k_{\mathrm{B}} 4\pi r^2 \left(C - P_{\mathrm{B}}/H\right). \tag{4}$$

The change in volume of the bubble over time can be represented as

$$\frac{\partial V}{\partial t} = 4\pi r^2 \frac{\partial r}{\partial t}, \tag{5}$$

and the derivative of the bubble's internal pressure with respect to time is given by

$$\frac{\partial P_B}{\partial t} = \rho_{\mathrm{w}} g \frac{\partial z}{\partial t} - \frac{2\sigma}{r^2}\frac{\partial r}{\partial t}. \tag{6}$$

Substituting the above formulas into the ideal gas law equation (1) yields the expression for the change of bubble radius over time as

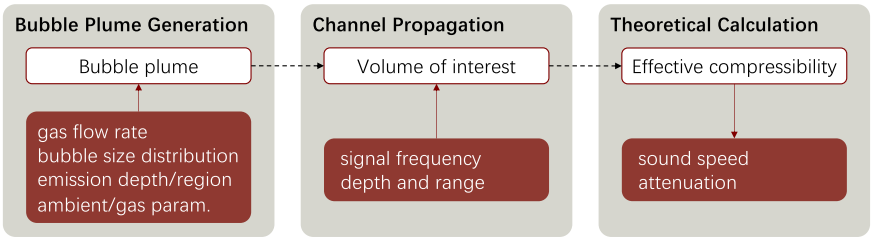

Fig. 1. Block diagram of the numerical model. The model comprises three parts. The bubble plume generation part generates simulated bubbles in the water column, which forms a gas plume. As the acoustic wave with a certain frequency propagates through the plume, a certain volume of interest is chosen and used as input for the theoretical calculation part. The last part incorporates the effective compressibility theory and outputs the sound speed.

$$\frac{\partial r}{\partial t} = \frac{RT\left(4\pi r^2 k_{\mathrm{B}}\left(C - \frac{1}{H}\left(P_{\mathrm{A}} + \rho_w g z + \frac{2\sigma}{r}\right)\right)\right) + \frac{4}{3}\pi r^3 \rho_{\mathrm{w}} g v_{\mathrm{B}}}{\left\{\left(P_{\mathrm{A}} + \rho_{\mathrm{w}} g z + \frac{2\sigma}{r}\right)4\pi r^2 - \frac{8\sigma}{3}\pi r\right\}} \tag{7}$$

The only unknowns in the above formulation are the two functions the rise velocity of the bubble v_{B}, and the gas transfer velocity, k_{B}. These two are non-trivial functions of bubble radius, depending on whether the water is fresh or saline. Formulations for these functions can be obtained under some very restrictive conditions. For instance, Stoke's law can be used to estimate the rise time of very small bubbles. But these methods are too constrained to be of real practical use and formulations based on empirical observations for both v_{B} and k_{B} are employed. The bubble rise velocity v_{B} is parameterized by the following semi-empirical equation proposed by Fan and Tsuchiya [14],

$$v_{\mathrm{B}} = \left\{\left(\frac{\rho_{\mathrm{w}} g r^2}{3.68 M^{-0.038}\mu_B}\right)^{-b} + \left(\frac{a\sigma}{\rho_{\mathrm{w}} r} + gr\right)^{-b/2}\right\}^{-(1/b)}, \tag{8}$$

where a and b are two empirical coefficients, σ denotes the surface tension, μ_B denotes the bulk viscosity, and $M = g\mu_B^2\rho_{\mathrm{w}}^{-1}\sigma^{-3}$ denotes the dimensionless Morton number that is only dependent upon the liquid's physical properties. To parameterize gas transfer velocity, two cases are considered. For clean, spherical bubbles with a thin concentration boundary layer, the result is obtained numerically with the Hadamard–Rybczynski solution [9]:

$$k_{\mathrm{B}} = \left\{0.212\frac{D v_{\mathrm{B}}}{r}\right\}^{0.5}, \tag{9}$$

where D denotes the diffusion coefficient and v_{B} denotes bubble vertical velocity. Considering bubbles with a well-developed boundary layer, the above equation is inappropriate and the gas transfer velocity can be given by:

$$k_{\mathrm{B}} = \left\{\frac{2}{\pi}\left(1 - 2.89 Re^{-0.5}\right)\frac{D v_{\mathrm{B}}}{r}\right\}^{0.5}. \tag{10}$$

The Reynolds number Re is given by:

$$Re = 2 r v_{\mathrm{B}}/\mu_K, \tag{11}$$

where μ_K denotes the kinematic viscosity.

Depending on the properties of gas and surrounding water, a bubble may shrink until the radius reaches a preset threshold $\hat{r}$ and be removed from the gas plume, or grow along with decreasing hydrostatic pressure and finally reach the surface.

2.2. Variations of sound speed imposed by bubble plume

As an acoustic wave propagates through a certain volume of bubbly medium, it is multi-scattered by bubbles and the energy is absorbed and re-transmitted depending on its frequency, which leads to a change of phase velocity and attenuation. One way to model this physical process is to consider the compressibility variation induced by oscillating bubbles [30]. With the modeling of the gas plume, the time and space information of all bubbles can be obtained. The water column is subsequently divided into grids at various ranges and depths; in each grid, the gas volume fraction V_{g} can be calculated. Thereby, the effective compressibility of the bubble-water mixture can be expressed as [43]:

$$K_{\mathrm{eff}} = (1 - V_{\mathrm{g}})K_{\mathrm{w}} + V_{\mathrm{g}}\Delta K, \tag{12}$$

where K_{w} denotes the compressibility of bubble-free water and can be obtained using the Newton-Laplace formula $K_{\mathrm{w}} = 1/(\rho_{\mathrm{w}} c_{\mathrm{w}}^2)$, and ΔK is the compressibility variation induced by bubbles, which can be estimated by:

$$\Delta K = \frac{1}{\rho_{\mathrm{w}}\pi f^2}\int_{r_{\min}}^{r_{\max}} \frac{r \cdot n(r)}{(f_r/f)^2 - 1 + iR_{\mathrm{B}}/\omega m_{\mathrm{B}}} dr, \tag{13}$$

where $n(r)$ denotes the number of bubbles with the same radii r in the volume, m_{B} the equivalent mass of oscillating bubble, and R_{B} the mechanical resistance of oscillating bubble [29]. $\omega = 2\pi f$ denotes the angular frequency of incident acoustic wave. $r_{\min}$ and $r_{\max}$ denote the minimum and maximum radius a bubble can be quantified, respectively. The Minnaert resonance frequency for a bubble with radius r (in cm) is adopted here as [31]:

$$f_r = \frac{1}{2\pi r}\sqrt{\frac{3\gamma P}{\rho_{\mathrm{w}}}}, \tag{14}$$

where P denotes the ambient pressure and γ denotes the adiabatic index of gas inside the bubble. Let ρ_{g} denote the density of the gas, then the effective density of the bubbly water is

$$\rho_{\mathrm{eff}} = (1 - V_{\mathrm{g}})\rho_{\mathrm{w}} + V_{\mathrm{g}}\rho_{\mathrm{g}}. \tag{15}$$

Applying the Newton-Laplace formula leads to the effective complex sound speed of the air-bubble mixture [11]

$$c_{\mathrm{eff}}^{-2} = K_{\mathrm{eff}}\rho_{\mathrm{eff}}, \tag{16}$$

the real part of which gives the phase velocity

$$c_b = \mathrm{Re}\left\{c_{\mathrm{eff}}\right\}. \tag{17}$$

3. Sound speed quantification

The quantification of underwater sound speed can be achieved by measuring the time-of-flight of a sound wave over a known distance. As an acoustic signal is transmitted, denoted as $s(t)$, it is first received by the nearest positioned hydrophone, then passes through the bubbly water column, and is finally received by the further positioned hydrophone. Here we denote $y_1(t)$ the acoustic signal received by the hydrophone close to the acoustic transducer and $y_2(t)$ the signal received by the hydrophone away from the transducer. Assuming that the gas plume does not significantly distort the time-domain waveform, the received waveform can be modeled as:

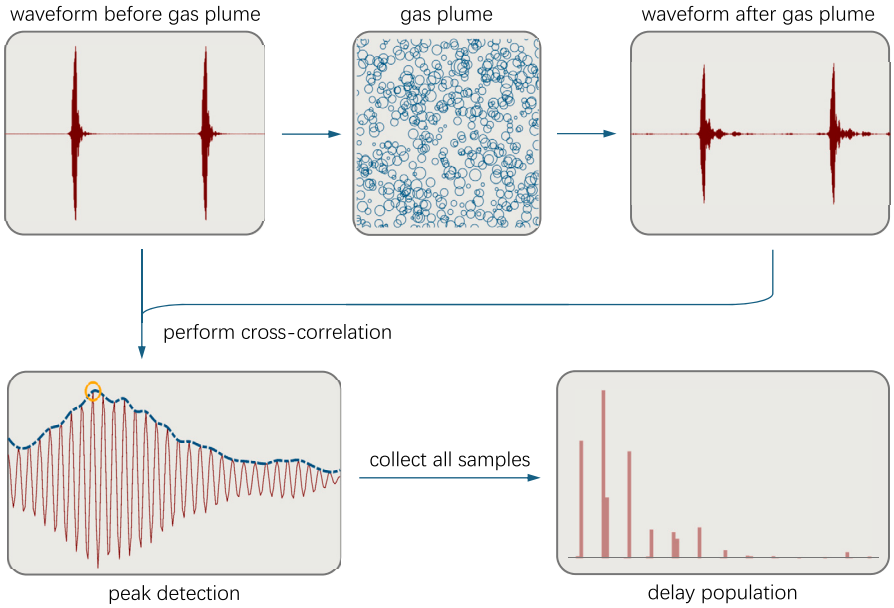

Fig. 2. Diagram of generating and processing the underwater acoustic signals. The waveform before and after passing through the gas plume is recorded to perform cross-correlation, the peak of which gives the estimate of propagation delay. Since a record contains a plethora of pulses and each pulse gives a sample of delay estimate, all the estimates again form a population which is used for the subsequent statistical process.

$$y_1(t) = A_1 s(t-\tau_1) + w_1(t),$$
$$y_2(t) = A_2 s(t-\tau_2) + w_2(t), \tag{18}$$

where $w_1(t)$ and $w_2(t)$ incorporate both ambient noise and sound emitted by bubbles, which are assumed mutually uncorrelated zero-mean stochastic processes. A_1, A_2 and τ_1, τ_2 are the unknown attenuated factors and propagation delays for the two hydrophones, respectively. Let Z denote the distance between the two hydrophones, then the sound speed is computed:

$$c = \frac{Z}{\tau_2 - \tau_1}. \tag{19}$$

Thus, the problem becomes to estimate the relative delay $\tau_0 = \tau_2 - \tau_1$, which is here achieved by a cross-correlation method described by

$$X_{12}(\tau) = A_1 A_2 X_{ss}\left(\tau - \tau_0\right), \tag{20}$$

where $X_{ss}(\tau)$, the auto-correlation function of the transmitted signal $s(t)$, taking the maximum value at $\tau = 0$. Consequently, the time delay is the value that maximizes the cross-correlation function

$$\tau_0 = \arg\max_{\tau} X_{12}(\tau), \quad \tau \in [\tau_{\min}, \tau_{\max}], \tag{21}$$

where $\tau_{\min}$ and $\tau_{\max}$ are the respective minimum and maximum possible values that the actual real time delay can reach.

Applying the above formulation to the analysis of experimental data requires two modifications. First, the waveform is recorded discretely at sampling frequency f_s the within finite observation time. As a result, $X_{12}(\tau)$ is not known precisely and only its discrete version can be estimated. A common practice to replace the cross-correlation function for an ergodic process is using its time-average function [7], defined by

$$\hat{X}_{12}[m] = \begin{cases} \frac{1}{L}\sum_{l=0}^{L-m-1} y_1[l]y_2[l+m], & m \geq 0 \\ \frac{1}{L}\sum_{l=-m}^{L-1} y_1[l]y_2[l+m], & m < 0 \end{cases} \tag{22}$$

where L denotes the length of the processed sequence. Thus, the estimate of time delay is given by

$$\hat{\tau}_0 = f_s \cdot \arg\max_{m} \hat{X}_{12}[m]. \tag{23}$$

Another modification is made in that the existence of cross-correlation function (20) requires the two signals to be wide-sense stationary (WSS) random processes, while the formation of the gas plume itself is essentially non-stationary. However, if the duration of the processed sequence is restricted to a relatively small window, the random signals can be viewed as WSS where the time scale of sound wave propagation is much less than bubble formation dynamics.

Fig. 3. Experimental scenario. The aluminum alloy frame carrying acoustic devices and air stones was suspended by a crane.

The entire data measurement file was divided into thousands of sample sequences in the stage of data processing and each sequence was used to obtain the time delay estimate $\hat{\tau}_0$ in (23). All estimates subsequently formed a population from which the true propagation time of acoustic waves could be inferred, and sound speed response to the gas plume was obtained immediately. Fig. 2 summarizes the algorithm presented above.

4. Anechoic tank experiment

This section illustrates the sound speed quantification experiment conducted in a large-scale anechoic tank. The tank is 50 m in length, 15 m in width, and 10 m in depth with anechoic materials fixed on its borders and removable anechoic tiles covering the water surface. The experimental scenario is shown in Fig. 3. Acoustic waves with frequencies from 1 to 100 kHz can be absorbed such that interference introduced by reverberation is minimized.

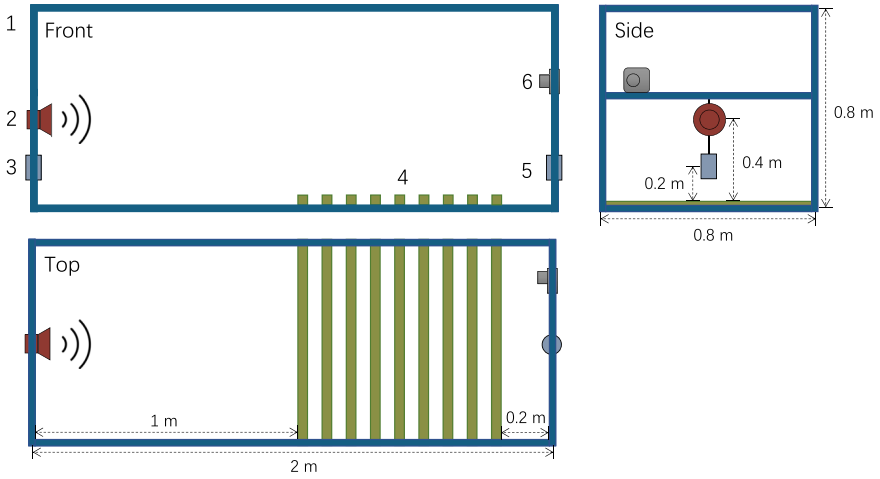

Fig. 4. Schematic of the experiment apparatus (underwater part). 1: Aluminum alloy frame; 2: Underwater speaker; 3: No.1 hydrophone; 4: Air stone diffuser (10 cm spacing); 5: No.2 hydrophone; 6: Underwater camera.

Table 1
Experimental conditions.

Experiment parameter	Value
LFM signal central frequency	1, 2, 4, 5, 6 & 8 kHz
LFM signal relative sweep range	central frequency ± 5%
LFM signal sweep time	2 ms
Pulse interval	48 ms
Flow rate	0, 0.2, 0.5 & 1 L/min
air stone depth	5 m

4.1. Experiment apparatus description

Fig. 4 exhibits the underwater part of the experiment apparatus. All devices were fixed on an aluminum alloy frame of 2 m in length, 0.8 m in width, and 0.8 m in height. Moreover, the frame also provides hanging points for the crane. To investigate sound speed variation around the bubble resonance frequency, an underwater speaker (Chungson ACE-900), whose effective frequency ranges from 80 Hz to 20 kHz, was used. The short propagation distance (2 m in the experiment) allowed the usage of the low source level (about 103 dB re μPa at 1 m) wide-band speaker. Nine commercial air stones (Hisin air stone, 80 cm in length with 80-120 mesh) were positioned at 1 m away from the speaker with 10 cm spacing to form a gas plume. Each air stone has two air inlets and a total of eighteen inlets were connected to a single air hose, which was subsequently connected to one end of a flowmeter (Siargo MF5706-25). An air compressor (Yangzi YZ-KYJ) outside the tank was connected to another end of the flowmeter. Thus, different gas flow rates could be achieved by adjusting the valve at the air compressor and monitoring the read on the flowmeter. Two hydrophones (sensitivity: -168 dB re 1 V/μPa), one (3 in Fig. 4) fixed at one end of the frame below the underwater speaker and another (5 in Fig. 4) fixed on the other end of the frame, were connected to an acoustic recorder, respectively, and the signal waveforms before and after passing through the gas plume were sampled. The scene of gas plume formation could be observed by an underwater camera (GoPro Hero 5) as shown in Fig. 6.

4.2. Controlled gas flow rate experiment

In this experiment, the frame was hung in the water by crane such that the bubbles were formed at 5 m depth. LFM pulses with frequencies ranging from 1 to 8 kHz were used to measure sound speed as the gas flow rate changed. In each experiment group, a signal with a certain frequency band was transmitted and the gas flow rate was held steady for 6 minutes. Hence, a total of 24 data records were obtained for the 6 frequency bands and 4 flow rates. All experiment conditions are summarized in Table 1.

5. Results

This section presents the experimental results along with the modeling results for comparison. Typically, evaluating a numerical model requires quantified comparison with ground truth data generated with the same inputs. To obtain a reference BSD, we apply the single bubble identification technique developed by a previous work [26], which distinguishes bubble signatures in the spectrogram. Besides, an optical bubble identification method is also applied to complement the acoustic method. Thereafter, two comparison approaches, namely the “forward” approach and the “inverse” approach, are presented. The former takes the reference BSD as model input and compares the simulation results with the experimental data, and the latter inverts the BSD and compares that with the reference one.

5.1. Determination of bubble size distribution

To generate the bubble plume model, the BSD is required. In an ideal situation, the BSD as an input to the model is regarded as the distribution counted in the experiment. Since the technique [26] works in the condition of bubble signatures not overlapping in both frequency- and time-domain, bubble sound recorded using a single air stone at 0.5 L/min gas flow rate was used for example analysis. Fig. 5(a) displays a spectrogram example with detected bubbles indicated by orange boxes. The frequencies of all the detected bubbles in the entire recording are synthesized into a bubble frequency histogram, as shown in Fig. 5(b). The dominant resonance frequency of the bubbles is approximately 4 kHz, which corresponds to bubbles with a radius of 1 mm at a water depth of 5 m. As the property of gas inside the bubble and the surrounding are assumed known, the bubble radius can be uniquely determined by the Minnaert formula (14), allowing to quantify the BSD.

To complement the acoustic method, we present an optical method for analyzing the video recorded during the experiment. The optical method involves the detection and tracking of bubbles, as well as a post-processing step to recover bubble radii from the tracked data. In the stage of detection, an average background is calculated by averaging a large number of frames without the presence of bubbles. This average background is then converted to gray scale, sharpened, and subjected to edge detection, which is used for background subtraction. Subsequently, the frames containing bubbles undergo the following procedure: conversion to gray scale, edge detection, and background subtraction. After the background subtraction, each frame is Gaussian

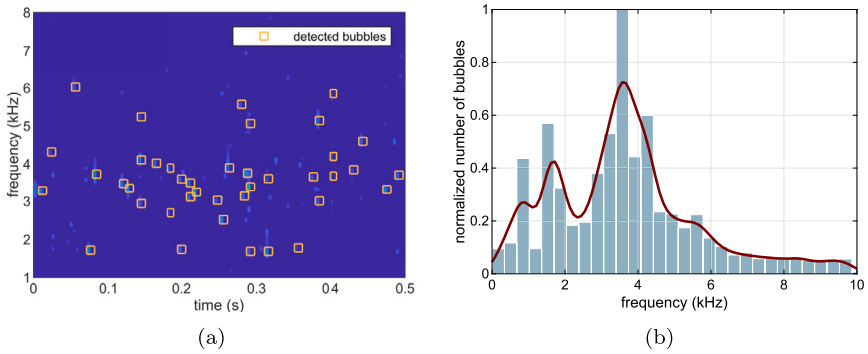

Fig. 5. (a) Bubbles detected on the time-frequency plane (orange boxes); (b) Histogram of bubble sound frequencies.

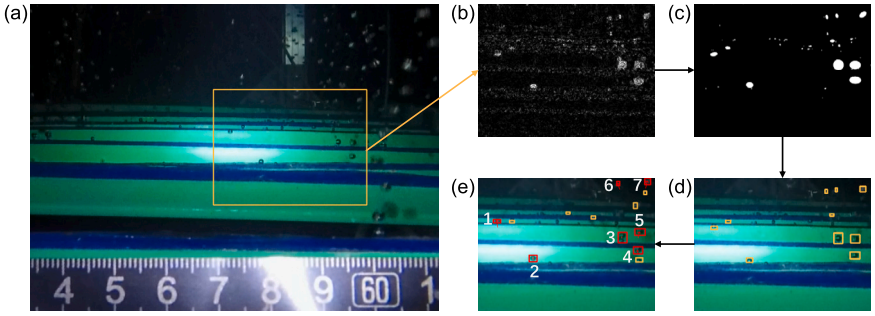

Fig. 6. Illustration of optical bubble identification. (a) Observed gas plume formation during the experiment; (b) Zoomed-in frame after edge detection and background subtraction; (c) Zoomed-in frame after image thresholding and flood filling; (d) Detected bubbles indicated by orange boxes; (e) Seven bubbles are successfully tracked in the frame, indicated by red boxes with arrows showing their movements relative to the previous frame. Their horizontal distances from the camera are determined based on their initial detected positions. Their radii are then converted from pixels to millimeters using the corresponding horizontal distances. The results are as follows: (horizontal distance, radius) 1: 42.1 cm, 0.8 mm; 2: 30.7 cm, 0.9 mm; 3: 40.9 cm, 1.2 mm; 4: 30.5 cm, 1.1 mm; 5: 30.9 cm, 1.0 mm; 6: 76.8 cm, 1.2 mm; 7: 61.2 cm, 1.3 mm.

blurred and converted to a binary image. A flood-filling algorithm is then applied to fill the hollows in the bubble edges. The binary image is subjected to connected component analysis, where components that satisfy shape and area criteria are recognized as candidates for bubbles. To associate candidates in two consecutive frames, a movement constraint is applied. In the latter frame, each candidate searches for the nearest candidate detected in the former frame, considering distance and moving direction to satisfy the movement constraint. The bubble detection and tracking procedure is illustrated in Fig. 6. Each tracked candidate is assigned a unique ID and recorded along with its detected positions across frames. Only candidates tracked for more than three frames are considered as true bubbles, while others are regarded as interferences. The depth of field for each detected bubble is determined based on its first detection coordinate, allowing the conversion of bubble radius from pixels to millimeters.

The BSDs obtained through the acoustic and optical methods are presented as probability normalized histograms and compared in Fig. 7. A notable observation is that the peak radius of the optical method is smaller than that of the acoustic method, and the BSDs obtained through the optical method are more evenly distributed. This discrepancy can be attributed to certain limitations inherent in the optical method. In areas where the illumination conditions are poor, the accuracy of radius measurements may be compromised. Consequently, the detected bubble edges during the edge detection stage might appear smaller than their actual size, leading to an increased number of smaller bubbles. Moreover, when multiple bubbles overlap, they can be detected as a single entity, resulting in an overestimation of the radius. This phenomenon contributes to the larger radius estimation results obtained through the optical method. Considering these factors, the BSD obtained through the acoustic method serves as model input as well as ground truth reference in the subsequent analysis, acknowledging its comparatively more reliable measurements.

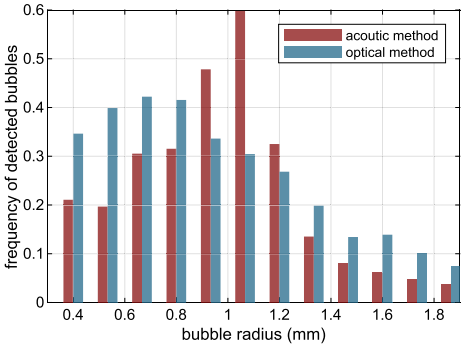

Fig. 7. Probability-normalized histograms obtained through the acoustic and optical method.

5.2. Forward comparison

Fig. 8 indicates the comparison between the model output and experiment results. After eliminating outliers in the population obtained using the method described in Section 3, propagation delay is estimated by calculating the average and subsequently dividing the propagation distance to obtain the sound speed. Note that sound speed has been calibrated such that sound speed without the presence of bubbles is a constant. The associated standard deviations are also calculated and displayed in Fig. 8 using vertical bars. As the true underlying bubble radius distribution in the experiment is not possible to gather, the model used the reference distribution described in Section 5.1 with the corresponding flux rate as input. The simulated sound speed variation curves are obtained by averaging the sound speed at 100 different time points during the model running. The results show that the simulated curves

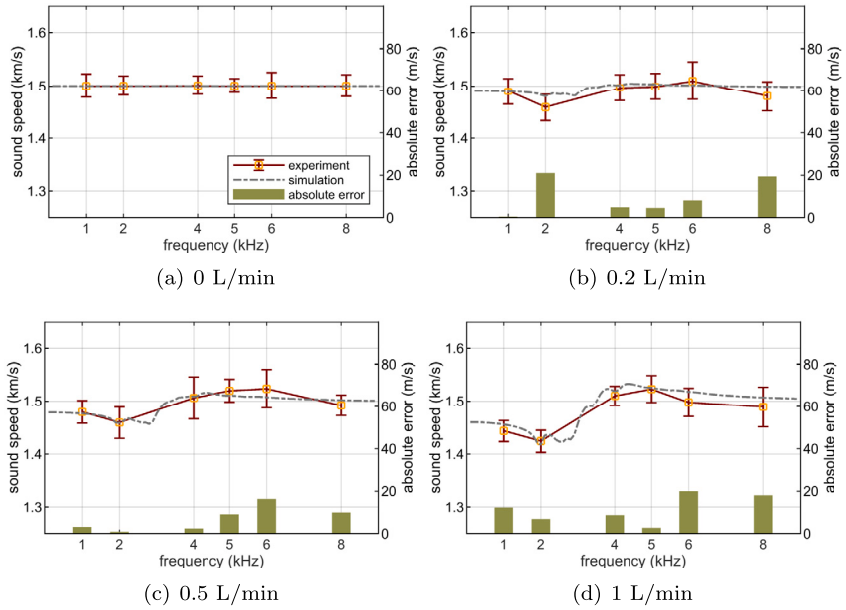

Fig. 8. Comparison between experiment results and simulation results at different flow rates. Data standard deviations are displayed as vertical bars at individual experimental data points. The simulation results are basically within the range of the standard deviation of the experiment results. The olive green bars indicate the absolute error.

Table 2
Modeling error evaluation. The model has minimum MAE and MAPE values at a flow rate of 0.5 L/min while having a maximum R-squared score at 1 L/min.

Metrics	0.2 L/min	0.5 L/min	1 L/min	Average
MAE (m/s)	9.75	**6.92**	11.40	9.36
MAPE (%)	0.66	**0.46**	0.77	0.63
R-squared (%)	41.98	84.96	**86.80**	71.25

(represented by gray dashed lines), which are basically within the standard deviation of measurements, exhibit good agreement with the experiment results. To quantify the modeling error, three metrics (i.e., Mean Absolute Error (MAE), Mean Absolute Percentage Error (MAPE), and R-Squared score, respectively [1]) are applied and the results are listed in Table 2.

The MAE expresses the average model prediction error and gives a sense of model accuracy. The minimum MAE is achieved at 0.5 L/min with a value of 6.92 m/s. The average MAE of all three flow rates is 9.36 m/s which corresponds to 0.63% percentage error. Although the errors are relatively small, it is not enough to suggest that the model is accurate, since the variation of sound speed is small, especially at low flow rates. Thereby, the R-squared score, which could reveal the proportion of the variation in the dependent variable predictable from the model, is further applied. The results indicate the model can explain the utmost 86.80% variation of the experimental data.

5.3. Inverse comparison

Another approach to validate the model is inverting the model input given the experimental data and comparing that with the reference one. Thereby a BSD inversion algorithm is developed here to provide auxiliary verification besides the forward comparison described above. Only the last two parts of the entire model (see Fig. 1) are used in the inversion procedure, which means that the gas plume generation procedure is deprecated and the radii of all bubbles in a certain volume are used as the model input. Since a cost function can be defined as the divergence between experimental data and model output, this inversion problem can be solved by global optimization techniques. Here, the Genetic Algorithm (GA) [19,41] is adopted as the framework of the inversion algorithm. The environment parameters required by the model, including the properties of inside gas and outside water of bubbles, are first established. The sound speed measurements are then interpolated to a high dimensional sound speed vector $\mathbf{c}_0$, which helps to improve the numerical stability. The variable to be solved in the inversion is set as the count vector of bubbles within different radius intervals denoted as $\mathbf{n}$. For each $\mathbf{n}$ generated in the algorithm, the corresponding bubble radius population is recovered and inputted into the forward model. This results in a theoretical sound speed vector $\mathbf{c}$, which is compared to the interpolated experimental sound speed vector $\mathbf{c}_0$ to calculate the fitness of the individual. And the fitness is defined as the Euclidean distance between the two vectors. The whole algorithm is detailed in Algorithm 1.

Fig. 9 displays the results obtained from running the GA algorithm. Similar to the previous section, ground truth data is lacking to quantify the inversion error and only a reference distribution provides a baseline for comparing. The histogram has been normalized for better visual comparison. All four histograms follow a similar pattern and the dominant bubble radius is around 0.9 mm. And the total number of bubbles obtained by inversion is roughly proportional to the corresponding gas flow rate. That is, by matching the model output with the experimental data, reasonable BSD, compared with the reference distribution, can be obtained, which confirms the validity of the model from another perspective.

Algorithm 1 BSD inversion algorithm based on GA.

1: set up model environment parameters
2: interpolate experiment measurements to high dimensional target sound speed vector $\mathbf{c}_0$
3: assign the number of generations to 0 (t = 0)
4: randomly create individuals in initial population $P(0)$ ▷ The individual is bubble radius count vector $\mathbf{n}$
5: **while** termination criterion is not satisfied **do**
6: $t = t + 1$
7: **for all** individuals **do**
8: recover bubble radius population from histogram bin count $\mathbf{n}$.
9: run forward model and obtain sound speed vector $\mathbf{c}$
10: individual fitness $\leftarrow \|\mathbf{c}_0 - \mathbf{c}\|_2$
11: **end for**
12: select individuals to next generation
13: change individuals using crossover and mutation
14: **end while**

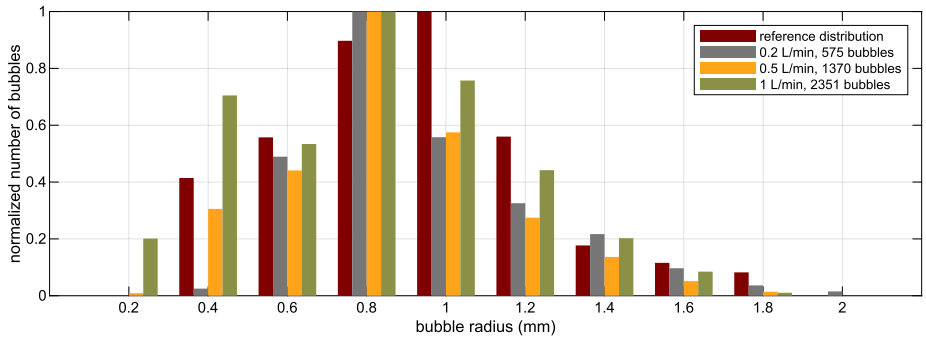

Fig. 9. Histogram of reference distribution and inversion results at the three flow rates (normalized). The results show that the four histograms share a similar pattern, where bubbles with a radius of 0.9 mm dominate. The total number of bubbles obtained by inversion is roughly proportional to the corresponding gas flow rate.

6. Discussion

6.1. Experiment limitations

Here, we first discuss two factors that could potentially introduce experimental errors. First, bubble liquids exhibit high dispersion and can cause discrepancies between group and phase speeds. In order to determine the sound speed response of bubbly liquids, it becomes necessary to measure the phase speed. In an ideal scenario, a continuous wave (CW) tone of a single frequency should be transmitted to ensure that the signal passing through the bubbly liquid possesses a pulsed frequency spectrum. However, the duration of the CW tone cannot be extended significantly due to the stochastic nature of upwelling bubbles. The CW tone's duration must be shorter than the time it takes for bubbles to exhibit significant movement. This constraint implies that the CW tone may experience spectrum leakage, resulting in an imperfect narrowband spectrum. Taking these factors into consideration, we chose to transmit narrowband LFM chirps, albeit at the expense of compromising the frequency band. This trade-off was made in order to achieve a higher level of accuracy in time delay estimation. Second, in the experiment, the monitoring hydrophone (3 in Fig. 4) was placed to the side of the source instead of in front it along the source-receive axis. This decision was made for two reasons: the underwater speaker used is omnidirectional, where the beams (and the strength of these beams) are equally spaced in front and side of the source which wound not introduce much influence on the measurements; the distance between the source (2 in Fig. 4) and the hydrophone (5 in Fig. 4) is small, which means less tolerance for the distance error. Placing hydrophone (3) on the path of direct sound propagation ray may introduce obstacles in the propagation channel, e.g., sound reflection, thus influence the sound speed measurements (highly possible).

We also notice three differences between the model and the experiment. In the experiment, we measured the phase speed of acoustic waves, which can be understood from the lens of the superposition of excitation sound waves and the sound waves generated by bubble vibrations. The frequency of excitation sound waves ranges from 1 to 8 kHz. As these acoustic waves encounter bubbles, they induce oscillations that generate additional sound waves where the dominant bubble vibration frequency is around 4 kHz. This generation can lead to either constructive or destructive interference with the incident waves, resulting in complex wave propagation phenomena. To simplify this complexity, the model we proposed leverages the effective compressibility theory. This approach helps to circumvent the complications introduced by the multi-scattering of acoustic waves, providing a more manageable analysis of the acoustic wave propagation in the presence of bubbles. The second difference lies in that the true gas plume generation dynamic in the experiment was not recovered as the model input. Whenever the pressure of air injected into the air hose changed, the bubbles could be emitted from different pockmarks at the sediment (here, the air stone) surface. The ever-changing bubble generation dynamic leads to the second difference, which is the uneven bubble spatial distribution. The effective compressibility theory takes the bubble-water mixture as a dispersive entirety whose compressibility changes along with bubbles. Moreover, the sound rays are assumed to pass through the bubbly region. While bubbles in the experiment were dispersed in several regions but uneven in the entire volume and the direct sound ray might not interact with these regions, which introduces uncertainty to the modeling. Hence, the model input flow rates were scaled down to fit the actual situation and the direct association between flow rate and sound speed variation is thus weak. When the proposed model is implemented and applied in the field work, more would need to be considered focusing on the various influence parameters from the environment.

6.2. Prospects for model refinement

The proposed model used Minneart frequency to calculate bubble resonance frequency in bubble plumes. The application of the Minnaert formula can be applied to isolated bubbles without interacting with each other. The interactions between bubbles is a common question in this research field and should be more comprehensively discussed and resolved. In our current investigation, we did not consider such interaction and acknowledged that may introduce some error. Furthermore, there exists a mutual influence between bubble resonance and acoustic transmission. When a bubble is generated and break the neck of gas tube between the bubble and leaking hole, it oscillates and radiates acoustic wave at the resonance frequency. This process may be affected by the incentive sound wave particularly when the incentive acoustic frequency is close to the bubble resonance frequency. Moreover, the incentive wave has an impact on the excitation of bubble walls and may change the shape of bubble. Such an impact may further alter the natural frequency of the bubble. In this study, we did not detail this scenario because we are more focused on the active acoustics rather than the passive sound radiated by the bubble generation.

The intricacies of bubble dynamics, including the effects of external acoustic waves on bubble behavior and the subsequent implications for both bubble resonance and acoustic transmission, represent critical areas for future research. By delving deeper into these aspects, subsequent studies could significantly enhance our understanding of the complex interactions at play, thereby refining the predictive capabilities of the proposed model.

6.3. BSD estimation technique comparison

In this investigation, we employed three distinct techniques for the estimation of BSD, namely the passive acoustic, optical, and the active acoustic inversion, each selected in accordance with specific considerations. The passive acoustic and optical techniques entail the direct analysis of acoustic signals and morphological characteristics of bubbles,

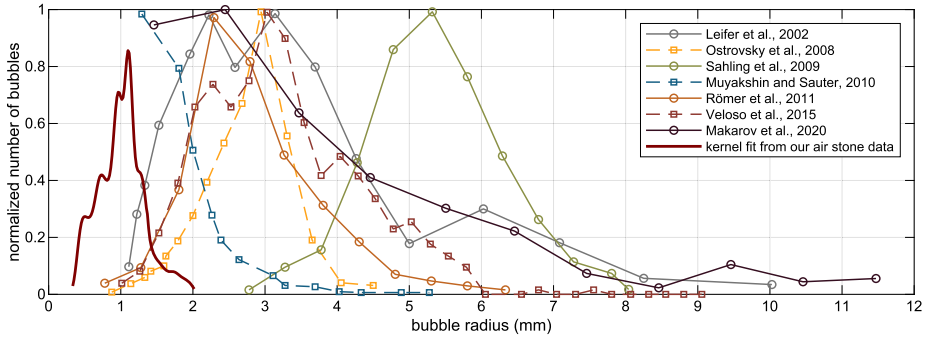

Fig. 10. Comparison between the experiment BSD and distributions in notable relevant works of literature. The bubbles emitted from the air stones are normally smaller than bubbles observed at natural underwater gas leakage sites, however, still in reasonable sizes.

Table 3
Compilation of underwater gas seepage found in natural environment. The associated BSDs are shown in Fig. 10 and compared with the BSD in our experiment.

Reference	Area	Seeping depth
[22]	Santa Barbara Channel	20 - 70 m
[33]	Lake Kinneret	36.5 - 43 m
[39]	Vodyanitskii mud volcano	about 2070 m
[32]	Haakon–Mosby mud volcano	about 1280 m
[37]	offshore Pakistan	400 - 3000 m
[44]	offshore NW-Svalbard	200 - 400 m
[28]	Lake Baikal	about 40 m

respectively. The passive acoustic method identifies bubble signatures in time-frequency spectrum, and forms a histogram of bubble radius by applying the Minnaert equation. The histogram is then used to obtain an estimation of BSD. We additionally incorporate an optical technique, utilizing video analysis for direct identification of bubbles, which offers a more visible estimation of BSD. The utilization of multiple estimation way can substantially increase the efficacy of the acoustic methods in this work. In contrast, the active acoustic inversion method operates indirectly by utilizing sound speed variations as input data for BSD estimation. The efficacy of the inversion method is contingent upon the precision of the underlying model. When the model accurately predicts sound speed variations, the inversion method yields favorable results. In turn, if the active acoustic inversion method demonstrates commendable performance, it substantiates the fidelity of the model. The passive acoustic method has proven to be effective for estimating BSD in both artificial and natural seepage environments [24,36]. However, the optical method may exhibit diminished performance in the presence of varying illumination conditions, as elucidated in Section 5. As a result, within the scope of this study, the passive method was employed to establish the ground truth BSD, while the optical method provided supplementary validation of the BSD. The inversion method served as a means of 'inverse comparison', thereby validating the reliability of the model. As indicated by the results, the model's accuracy is evident, affirming the inversion method's competence in the precise estimation of BSD.

6.4. BSD in natural environment

As the objective of the developed model resides in its capacity to predict sound speed and attenuation at real world underwater gas leakage sites, it becomes imperative to engage in a comparison between the BSD observed in the experiment and the BSD inherent to natural underwater environments. Table 3 lists notable relevant literature concerning underwater gas leakage and the corresponding BSDs are shown in Fig. 10 in comparison with the BSD estimated from our air stone data. This comparison reveals substantial variations in bubble size across different geographical locations. The bubbles generated within our experiment exhibit smaller dimensions when compared with those observed in natural marine ecosystems, albeit remaining within a reasonable range. The dominant bubble radius, determined to be approximately 1.1 mm in our study, closely aligns with findings reported by Muyakshin and Sauter [32]. Consequently, it can be reasonably asserted that the BSD in our experiment is a credible and informative proxy for representing the BSD in natural underwater environments.

7. Conclusion

In this paper, we developed a numerical model to simulate the underwater sound speed variation imposed by the gas plume. By transmitting LFM pulses at six frequencies centered ranging from 1 to 8 kHz through gas plumes generated at various flow rates, the propagation delays were estimated using time-domain correlation, and the sound speeds were obtained by processing these delays statistically. The experimental measurements exhibit consistency with the model output and the average MAE is 11.53 m/s with a 72.2% R-Squared score. A BSD inversion algorithm based on GA was developed to match the model output and the experimental data. This algorithm serves as an additional validation tool for the numerical model, reinforcing confidence in the effectiveness of the developed model. These collective findings underscore the potential for leveraging active acoustic monitoring techniques for the surveillance and assessment of underwater gas emissions, thus contributing to the advancements in underwater acoustic characterization of gas plumes and marine environmental monitoring.

CRediT authorship contribution statement

Shuduo Liu: Data curation, Software, Writing – original draft. **Jianghui Li:** Conceptualization, Methodology, Writing – review & editing. **Wen Xu:** Resources, Writing – review & editing.

Declaration of competing interest

The authors declare the following financial interests/personal relationships which may be considered as potential competing interests: Wen Xu reports financial support was provided by National Natural Science Foundation of China.

Data availability

The authors do not have permission to share data.

Acknowledgement

This research is financially supported by the National Natural Science Foundation of China Grant No. 61831020 and the Natural Science Foundation of Xiamen, China Grant No. 3502Z202373006. The authors would like to thank Prof. P. R. White, Dr M. Liu, and Miss Y. Wu, who have provided substantial support for data collection and theoretical analysis.

References

[1] Bingham NH, Fry JM. Regression: linear models in statistics. Springer Science & Business Media; 2010.

[2] Blackford J, Stahl H, Bull JM, Bergès BJP, Cevatoglu M, Lichtschlag A, et al. Detection and impacts of leakage from sub-seafloor deep geological carbon dioxide storage. Nat Clim Change 2014;4:1011–6. https://doi.org/10.1038/nclimate2381.

[3] Brennen CE. Cavitation and bubble dynamics. Cambridge: Cambridge University Press; 2013.

[4] Buckingham MJ. Sound speed and void fraction profiles in the sea surface bubble layer. Appl Acoust 1997;51:225–50. https://doi.org/10.1016/S0003-682X(97)00002-9.

[5] Caflisch RE, Miksis MJ, Papanicolaou GC, Ting L. Effective equations for wave propagation in bubbly liquids. J Fluid Mech 1985;153:259–73. https://doi.org/10.1017/S0022112085001252.

[6] Caudron C, Vandemeulebrouck J, Sohn RA. Turbulence-induced bubble nucleation in hydrothermal fluids beneath Yellowstone Lake. Commun Earth Environ 2022;3:1–6. https://doi.org/10.1038/s43247-022-00417-6.

[7] Chen J, Benesty J, Huang Y. Time delay estimation in room acoustic environments: an overview. EURASIP J Adv Signal Process 2006;2006:026503. https://doi.org/10.1155/ASP/2006/26503.

[8] Cheyne SA, Thurman HO, Tiblin CM. The inferred determination of the phase speed of a bubbly liquid of less than 2 m/s by using a transfer function technique. J Acoust Soc Am 2019;146:1834–8. https://doi.org/10.1121/1.5126864.

[9] Clift R, Grace JR, Weber ME. Bubbles, drops, and particles. Chelmsford, Massachusetts: Courier Corporation; 2005.

[10] Commander KW, Prosperetti A. Linear pressure waves in bubbly liquids: comparison between theory and experiments. J Acoust Soc Am 1989;85:732–46. https://doi.org/10.1121/1.397599.

[11] Crawford FS. The hot chocolate effect. Am J Phys 1982;50:398–404. https://doi.org/10.1119/1.13080.

[12] Duro V, Rajaona DR, Décultot D, Maze G. Experimental study of sound propagation through bubbly water: comparison with optical measurements. IEEE J Ocean Eng 2011;36:114–25. https://doi.org/10.1109/JOE.2010.2096971.

[13] Esposito C, Yenigun O, Gouriet JB, Steelant J, Vetrano MR. Void fraction and speed of sound measurement in cavitating flows by the three pressure transducers (3PT) technique. Exp Therm Fluid Sci 2020;112:109949.

[14] Fan LS, Tsuchiya K. Bubble wake dynamics in liquids and liquid-solid suspensions. Waltham, Massachusetts: Butterworth-Heinemann; 2013.

[15] Farmer DM, Vagle S. Waveguide propagation of ambient sound in the ocean-surface bubble layer. J Acoust Soc Am 1989;86:1897–908. https://doi.org/10.1121/1.398568.

[16] Feuillade C. The attenuation and dispersion of sound in water containing multiply interacting air bubbles. J Acoust Soc Am 1996;99:3412–30. https://doi.org/10.1121/1.415216.

[17] Foldy LL. The multiple scattering of waves. I. General theory of isotropic scattering by randomly distributed scatterers. Phys Rev 1945;67:107–19. https://doi.org/10.1103/PhysRev.67.107.

[18] Fox FE, Curley SR, Larson GS. Phase velocity and absorption measurements in water containing air bubbles. J Acoust Soc Am 1955;27:534–9. https://doi.org/10.1121/1.1907955.

[19] Holland JH. Adaptation in natural and artificial systems: an introductory analysis with applications to biology, control, and artificial intelligence. Complex adaptive systems. Cambridge, MA, USA: A Bradford Book; 1992.

[20] Koltsova I, Krynskii L, Mikhailov I, Pokrovskaya I. Attenuation of ultrasonic-waves in low-viscosity liquids containing gas-bubbles. Sov Phys Acoust USSR 1979;25:409–13.

[21] Leifer I, Culling D. Formation of seep bubble plumes in the Coal Oil Point seep field. Geo Mar Lett 2010;30:339–53. https://doi.org/10.1007/s00367-010-0187-x.

[22] Leifer I, Judd AG. Oceanic methane layers: the hydrocarbon seep bubble deposition hypothesis. Terra Nova 2002;14:417–24. https://doi.org/10.1046/j.1365-3121.2002.00442.x.

[23] Leifer I, Patro RK. The bubble mechanism for methane transport from the shallow sea bed to the surface: a review and sensitivity study. Cont Shelf Res 2002;22:2409–28. https://doi.org/10.1016/S0278-4343(02)00065-1.

[24] Li J, Roche B, Bull JM, White PR, Davis JW, Deponte M, et al. Passive acoustic monitoring of a natural CO_2 seep site – implications for carbon capture and storage. Int J Greenh Gas Control 2020;93:102899. https://doi.org/10.1016/j.ijggc.2019.102899.

[25] Li J, White PR, Bull JM, Leighton TG, Roche B. A model for variations of sound speed and attenuation from seabed gas emissions. In: OCEANS 2019 MTS/IEEE SEATTLE; 2019. p. 1–9.

[26] Li J, White PR, Roche B, Bull JM, Leighton TG, Davis JW, et al. Acoustic and optical determination of bubble size distributions – quantification of seabed gas emissions. Int J Greenh Gas Control 2021;108:103313. https://doi.org/10.1016/j.ijggc.2021.103313.

[27] Macpherson JD. The effect of gas bubbles on sound propagation in water. Proc Phys Soc B 1957;70:85. https://doi.org/10.1088/0370-1301/70/1/312.

[28] Makarov MM, Muyakshin SI, Kucher KM, Aslamov IA, Granin NG. A study of the gas seep Istok in the Selenga shoal using active acoustic, passive acoustic and optical methods. J Great Lakes Res 2020;46:95–101. https://doi.org/10.1016/j.jglr.2019.10.014.

[29] Medwin H. Acoustic fluctuations due to microbubbles in the near-surface ocean. J Acoust Soc Am 1974;56:1100–4. https://doi.org/10.1121/1.1903391.

[30] Medwin H, Clay CS. Chapter 8 - Bubbles. In: Medwin H, Clay CS, editors. Fundamentals of acoustical oceanography. Applications of modern acoustics. San Diego: Academic Press; 1998. p. 287–347.

[31] Minnaert M. XVI. On musical air-bubbles and the sounds of running water. Lond Edinb Dublin Philos Mag J Sci 1933;16:235–48. https://doi.org/10.1080/14786443309462277.

[32] Muyakshin SI, Sauter E. The hydroacoustic method for the quantification of the gas flux from a submersed bubble plume. Oceanology 2010;50:995–1001.

[33] Ostrovsky I, McGinnis DF, Lapidus L, Eckert W. Quantifying gas ebullition with echosounder: the role of methane transport by bubbles in a medium-sized lake. Limnol Oceanogr, Methods 2008;6:105–18.

[34] Prosperetti A, Crum LA, Commander KW. Nonlinear bubble dynamics. J Acoust Soc Am 1988;83:502–14. https://doi.org/10.1121/1.396145.

[35] Reeder DB, Joseph JE, Rago TA, Bullard JM, Honegger D, Haller MC. Acoustic spectrometry of bubbles in an estuarine front: sound speed dispersion, void fraction, and bubble density. J Acoust Soc Am 2022;151:2429–43. https://doi.org/10.1121/10.0009923.

[36] Roche B, White PR, Bull JM, Leighton TG, Li J, Christie C, et al. Methods of acoustic gas flux inversion—investigation into the initial amplitude of bubble excitation. J Acoust Soc Am 2022;152:799–806.

[37] Römer M, Sahling H, Spieß V, Bohrmann G. The role of gas bubble emissions at deep-water cold seep systems: an example from the Makran continental margin, offshore Pakistan. In: Proceedings of the 7th international conference on gas hydrates (ICGH 2011), Edinburgh, Scotland, United Kingdom; 2011.

[38] Ruggles AE, Lahey Jr RT, Drew DA, Scarton HA. An investigation of the propagation of pressure perturbations in bubbly air/water flows. J Heat Transf 1988;110:494–9. https://doi.org/10.1115/1.3250513.

[39] Sahling H, Bohrmann G, Artemov YG, Bahr A, Brüning M, Klapp SA, et al. Vodyanitskii mud volcano, Sorokin trough, Black Sea: geological characterization and quantification of gas bubble streams. Mar Pet Geol 2009;26:1799–811.

[40] Silberman E. Sound velocity and attenuation in bubbly mixtures measured in standing wave tubes. J Acoust Soc Am 1957;29:925–33. https://doi.org/10.1121/1.1909101.

[41] Slowik A, Kwasnicka H. Evolutionary algorithms and their applications to engineering problems. Neural Comput Appl 2020;32:12363–79. https://doi.org/10.1007/s00521-020-04832-8.

[42] Sojahrood AJ, Haghi H, Karshfian R, Kolios MC. Probing the pressure dependence of sound speed and attenuation in bubbly media: experimental observations, a theoretical model and numerical calculations. Ultrason Sonochem 2023;106319.

[43] Urick RJ. Principles of underwater sound. 3rd edition. Originated 1983 edition ed. Los Altos, Calif: Peninsula Pub; 1996.

[44] Veloso M, Greinert J, Mienert J, De Batist M. A new methodology for quantifying bubble flow rates in deep water using splitbeam echosounders: examples from the Arctic offshore NW-Svalbard. Limnol Oceanogr, Methods 2015;13:267–87. https://doi.org/10.1002/lom3.10024.

[45] Wijngaarden LV. On the equations of motion for mixtures of liquid and gas bubbles. J Fluid Mech 1968;33:465–74. https://doi.org/10.1017/S002211206800145X.

[46] Wilson PS, Roy RA, Carey WM. Phase speed and attenuation in bubbly liquids inferred from impedance measurements near the individual bubble resonance frequency. J Acoust Soc Am 2005;117:1895–910. https://doi.org/10.1121/1.1859091.